JACS
JOURNAL OF THE AMERICAN CHEMICAL SOCIETY
Article
pubs.acs.org/JACS

First Principles Simulations of the Electrochemical Lithiation and Delithiation of Faceted Crystalline Silicon

Maria K. Y. Chan,*[,†] C. Wolverton,[‡] and Jeffrey P. Greeley*[,†]

[†]Center for Nanoscale Materials, Argonne National Laboratory, Argonne, Illinois 60439, United States
[‡]Materials Science Department, Northwestern University, Evanston, Illinois 60208, United States

Supporting Information

ABSTRACT: Silicon is of significant interest as a next-generation anode material for lithium-ion batteries due to its extremely high capacity. The reaction of lithium with crystalline silicon is known to present a rich range of phenomena, including electrochemical solid state amorphization, crystallization at full lithiation of a $Li_{15}Si_4$ phase, hysteresis in the first lithiation−delithiation cycle, and highly anisotropic lithiation in crystalline samples. Very little is known about these processes at an atomistic level, however. To provide fundamental insights into these issues, we develop and apply a first principles, history-dependent, lithium insertion and removal algorithm to model the process of lithiation and subsequent delithiation of crystalline Si. The simulations give a realistic atomistic picture of lithiation demonstrating, for the first time, the amorphization process and hinting at the formation of the $Li_{15}Si_4$ phase. Voltages obtained from the simulations show that lithiation of the (110) surface is thermodynamically more favorable than lithiation of the (100) or (111) surfaces, providing an explanation for the drastic lithiation anisotropy seen in experiments on Si micro- and nanostructures. Analysis of the delithiation and relithiation processes also provides insights into the underlying physics of the lithiation−delithiation hysteresis, thus providing firm conceptual foundations for future design of improved Si-based anodes for Li ion battery applications.

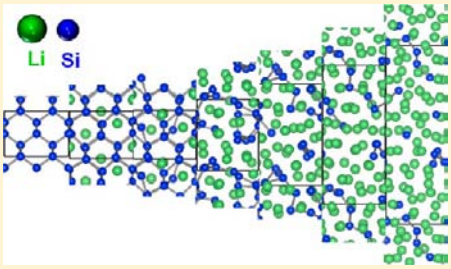

1. INTRODUCTION

Lithium-ion batteries are ubiquitous in consumer electronics, but the limited capacities of current Li-ion battery materials have so far limited deployment of this technology to the transportation sector. There are therefore substantial and ongoing research efforts to develop electrode materials with higher capacities. For the anode, silicon[1−3] has attracted widespread attention as an alternative to graphitic carbon due to its large gravimetric capacity, approaching 10 times that of graphite, as well as its large volumetric capacity, approximately 3 times that of graphite when considering the volumes after lithiation.

The lithiation of crystalline Si results in substantial structural changes, in significant contrast to transition metal oxides or graphitic electrode materials where Li is intercalated into lattice sites with limited structural distortions. One such structural change is the transformation, at room temperature, of crystalline Si into amorphous lithiated silicides (Li_xSi) during lithiation;[4,5] at higher temperatures (ca. 400 °C), in contrast, various crystalline Li_xSi phases form.[1] The measured voltages are substantially lower for the room temperature[5] than for the high temperature[1] electrochemical lithiation of crystalline Si at corresponding compositions (up to 0.2 V). The lack of formation of crystalline Li_xSi phases at room temperature is therefore most likely due to kinetic constraints, meaning that the room-temperature Li−Si reaction is a nonequilibrium process. The atomistic underpinnings of this nonequilibrium electrochemical amorphization process are of fundamental interest and have been extensively studied experimentally by, for example, X-ray diffraction (XRD),[6] nuclear magnetic resonance (NMR),[7,8] and electron energy loss spectroscopy (EELS).[9] Density functional theory (DFT) studies have analyzed dilute lithium insertion and diffusion in crystalline Si bulk,[10] thin films[11] and nanowires,[12,13] as well as the properties of crystalline Li_xSi phases[14,15] and the lithiation of bulk amorphous Si to form amorphous lithium silicides.[16−18] However, none of these studies has provided a comprehensive, atomic-level description of the amorphization of crystalline Si upon lithiation, and the development of such a description is a key unsolved problem in the Li−Si reaction. While DFT has been used to produce amorphous Li−Si structures at high temperature (900−1500 K),[19,20] at such high temperatures the Li−Si reaction is expected to produce crystalline bulk Li_xSi phases,[1] so the relevance of these amorphous Li−Si phases to lithiation of crystalline Si is unknown.

Another significant structural transformation that occurs during the Li−Si electrochemical reaction is the crystallization, from otherwise amorphous Li_xSi, of the $Li_{15}Si_4$ phase at the end of discharge.[21] The $Li_{15}Si_4$ phase is somewhat unstable and possibly nonstoichiometric ($Li_{15\pm\delta}Si_4$) due to electron-deficiency,[7] and its formation can be avoided by restricting the discharge cutoff voltage to 50 mV or greater.[22] While some properties of the ideal $Li_{15}Si_4$ phase have been explored by DFT,[15,23,24] there is indication that the local coordination in the material formed by solid state synthesis differs from that formed

Received: February 22, 2012
Published: July 21, 2012

   dx.doi.org/10.1021/ja301766z | J. Am. Chem. Soc. 2012, 134, 14362−14374

by electrochemical lithiation.[7] Therefore, simulations that give information on the details of the formation of this new phase during the lithiation process are highly desirable.

The large volumetric expansion of Si during lithiation, up to 300%, is another structural transformation that presents a key technological challenge to the implementation of silicon anodes.[25] Because of this expansion, the anode undergoes severe mechanical stress during cycling, resulting in pulverization. To counteract this volumetric expansion problem, various approaches have been attempted, including preconditioning cycles to partially lithiate each Si particle,[22] active phase dilution by alloying,[26] elastic binders to prevent mechanical separation,[27] nanoparticles connected to carbonaceous scaffolding to ensure connectivity while allowing for expansion,[28,29] nanowires to allow for expansion perpendicular to the wire directions,[30] and, recently, patterned microstructures to strain limit the amount of lithiation.[31]

The strain limitation approach, in particular, relies on large lithiation anisotropy between different crystal orientations of Si, a fascinating effect which has been observed for microstructures[31] and nanowires.[32,33] It was found that the expansion of the lithiated Si is vastly more preferable perpendicular to the (110) plane compared to the (111) plane. Kinetic[31,13] and mechanical[32] reasons have been offered as possible explanations for this effect, but it is unclear how differences in surface-to-subsurface diffusion barriers alone can lead to such drastic anisotropy in micrometer-sized structures, since the Li diffusion tensor should obey the cubic crystal symmetry just a few atomic layers away from the surface. Herein, we propose an alternative explanation for this important phenomenon.

In this work, we combine DFT calculations with a physically motivated, history-dependent lithium insertion algorithm to simulate the room temperature process of Li reaction with crystalline Si. The simulations allow us to obtain, from first principles, a detailed atomistic picture of the lithiation and amorphization processes. Tests of variations of the algorithm and corroborations of its predictions with available experimental Si–Si radial distribution functions demonstrate that the simulations provided robust and physically sensible descriptions of these processes. Using the simulations, we are able to distinguish the various stages of amorphization for the different crystalline orientations, as well as evolution of the Li–Si and Li–Li correlations. DFT total energies and atomistic configurations from the calculations further allow us to derive lithiation voltages, mechanical changes, and kinetic barriers for different crystalline orientations, from which we postulate a thermodynamic origin of the experimentally observed lithiation anisotropy. The thermodynamic explanation of the anisotropy is related to atomistic differences in the amorphization process, and circumvents problems with previous explanations. Finally, the delithiation and relithiation processes are also simulated in a similar way and the simulations point to the existence of hysteresis, for which we provide a simple physical explanation. Overall, the structural and energetic information determined from these investigations provides an unprecedented understanding of the atomistic details of Si lithiation and lays the foundations for future design of improved Si anodes for Li ion battery applications.

2. METHODS

2.1. Density Functional Theory Calculations. We perform DFT calculations using the Vienna Ab Initio Simulation Package (VASP),[34] with supplied Projector Augmented Wave (PAW) potentials for core electrons.[35] The generalized gradient approximation (GGA) of Perdew–Becke–Ernzerhof (PBE)[36] is used for the exchange-correlation functional. We use two different sets of parameters, one for configurational sampling ("fast"), and another for final relaxations and accurate total energy determination of the low energy structures that are determined from the fast sampling ("accurate"). For "fast" calculations, we use kinetic energy cutoffs of 270 eV for the plane wave basis set, a convergence criterion of 1 meV/cell for ionic relaxation, and Γ-centered grids of approximately 8000 $Å^3/V$ k-points, where V is the volume of the computational cell. The "accurate" calculations are performed with kinetic energy cutoffs of 340 eV, a convergence criterion of 0.1 meV/cell, and Γ-centered grids of approximately 27000 $Å^3/V$ k-points. "Fast" calculation parameters can introduce errors in distinguishing among structures with small energy differences, of order 10 meV/cell. The reference energy for metallic bcc Li is calculated using a kinetic energy cutoff of 340 eV and is converged with respect to k-point density to 0.2 meV/atom.

2.2. Models of Crystalline Si. We are interested in developing techniques to simulate the insertion of Li into micrometer-sized or larger Si particles that initially display well-defined surface facets; therefore, the use of single crystal surface models is appropriate. The silicon surfaces considered in this study are (100), (110), and (111). These are the most common crystallographic surfaces studied and the only such surfaces available for purchase as Si wafers. We consider low-energy surface cells, both nonreconstructed and reconstructed, consisting of two and four Si atoms per layer. For (100), we use the 2 × 1 and 2 × 2 symmetric-[37] and buckled-[38] dimer reconstructions, with two and four Si atoms per layer, respectively. For (110), we consider the unreconstructed surface in 1 × 1 and 1 × 2 cell sizes, again with two and four Si atoms per layer, respectively. For (111), the 2 × 1 reconstruction found for freshly cleaved surfaces,[39] and the 2 × 2 supercell thereof, as well as the unreconstructed surface with two and four atoms per layer, are used. The surface models are shown in Figure 1. The surface slabs are separated from their periodic images by a vacuum of at least 17 Å in thickness. In all calculations, the cell dimensions are fixed. For each surface orientation, we evaluate the surface cell and Li configurations corresponding to the highest-voltage surface-only lithiation,[40] and we then proceed with the lithiation and delithiation routines, as described below.

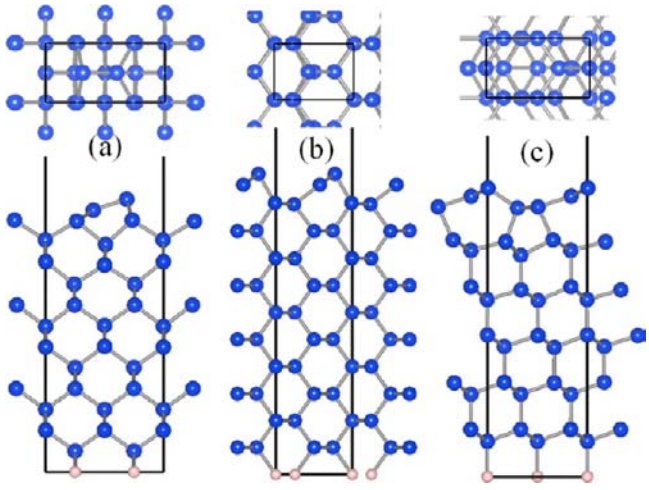

Figure 1. Top (top) and side (bottom) views of the surface cells used in this study: (a) Si (100) 2 × 1 with buckled dimers; (b) Si (110) 1 × 1 unreconstructed; and (c) Si (111) 2 × 1 reconstruction (ref 39). The larger (blue) spheres represent silicon atoms, while the smaller (pink) spheres represent hydrogen atoms used to passivate the bottom of the slabs. The black boxes represent the boundaries of the periodic computational cells. This and subsequent figures of atomistic structures in this manuscript are produced with the VESTA software.[41]

2.3. Lithiation and Delithiation Routines. As discussed in the Introduction, the first-cycle electrochemical lithiation of crystalline Si

at room temperature is a nonequilibrium process in which the crystalline Li_xSi phases, the thermodynamic ground states, do not form. Therefore, conventional techniques designed to find thermodynamic ground states, such as cluster expansions,[42] cannot be applied to determine intermediate configurations during the lithiation process. The physical process of Li insertion destroys the crystalline Si lattice, so a history-dependent approach must be taken to simulate the lithiation process, in order to find amorphous Li_xSi configurations which are mechanistically connected to the initially crystalline Si through the insertion of Li. We carry out such simulations using a step-by-step insertion of Li into Si. Chevrier and Dahn[16,17] also used a step-by-step Li insertion procedure, starting from amorphous Si, in which Li is inserted into the largest void within the computational cell at each step. However, in testing the insertion of Li into different interstitial sites, we find that the site farthest away from existing atoms is the most energetically favorable site after relaxations in only approximately 20% of all cases. Although there was some correlation between distance from existing atoms and energy before relaxation, the correlation is not strong and disappears after relaxation, as discussed in Supporting Information SI.0. Therefore, we modify the algorithm of Chevrier and Dahn to allow the insertion of Li into all possible interstitial sites, and we choose at each step the lowest energy configuration after relaxation for the insertion of the next Li. The details are described below and illustrated in Figure 2:

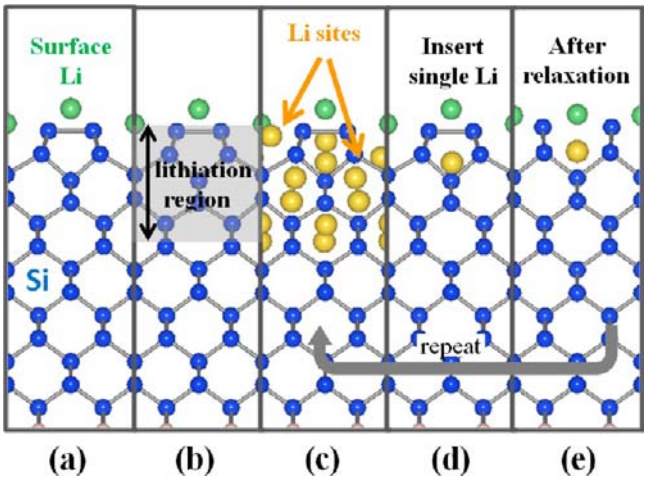

Figure 2. Schematic representation of the lithiation algorithm, using the Si (100) surface as an illustration. See text for details.

1. Using models with two and four Si atoms per layer, surface Li adsorption sites and the surface-only lithiation voltages are determined. The configuration corresponding to surface-only lithiation at the highest voltage (Figure 2a) is used as a starting point for further lithiation.
2. A slab of crystalline Si, corresponding to 5 layers of Si (with a thickness of 7−10 Å before lithiation), is identified, where Li insertion is allowed (Figure 2b). The Si below this slab remains unlithiated, and the Si atoms in the bottom-most 2−4 layers are fixed at the bulk Si lattice parameters to simulate the effect of bulk crystalline Si.
3. For each lithium atom inserted, we repeat the following steps:
   a. Using a regular spatial grid, we determine all interstitial sites $\{\mathbf{r}_i\}$ that are at least d_{min} from the nearest atoms. These sites are then ranked in descending order of the distance from the nearest atom. The first site on the list is selected as an insertion site. Each subsequent site is selected if it is at least d_{min} from the site(s) that have already been selected (Figure 2c).
   b. A lithium atom is inserted separately into each $\mathbf{r}_i$, and the total energy is calculated with ionic relaxations using "fast" parameters (see Section 2.1 for details) (Figure 2d).
   c. The lowest energy relaxed configuration is relaxed with "accurate" parameters and chosen for further lithium insertion (Figure 2e).

Note that d_{min} is an input parameter to the algorithm. The value of d_{min} is set to the largest value such that at least one interstitial site is found at all steps, which we found to be 1.9 Å. For comparison, typical relaxed Li−Si distances are between 2.4 and 2.6 Å.

Delithiation is simulated as the reverse of the above process. Taking the configuration with the most Li inserted that is thermodynamically stable with respect to the unlithiated Si surface and metallic Li, we remove the Li atoms one at a time. At each step, all possible removals are calculated using the "fast" parameters. Again, the lowest energy configuration is chosen, relaxed using the "accurate" parameters, and the process is repeated.

To elucidate the explicit effects of the solid-vacuum interface on our voltage curves, we also carry out lithiation simulations without such an interface present. The computational cells are constructed from bulk crystalline Si to include no vacuum, such that the vertical (z) axis is along the ⟨100⟩, ⟨110⟩, or ⟨111⟩ direction. The initial cells contain 16−24 Si atoms, with four per layer, and are of dimensions 5.5−9.5 Å. We carry out lithiation simulations as described above, except that:

1. Li can be inserted in any interstitial site and there is no layer of Si that is kept crystalline;
2. After each Li is inserted and the structure relaxed with fixed cell shape and volume, the lowest-energy configuration is chosen. For this configuration, the length of the cell in the z-direction is adjusted and relaxation carried out until the pressure on the cell in the z-direction is below 10^7 Pa (0.1 kbar) before the next Li is inserted.

As with simulations including the solid-vacuum interface, the lateral dimensions of the computational cells (the cross section in the $x-y$ plane) are kept fixed. The fixed lateral dimensions represent the constraints placed by the underlying crystal in a certain orientation, such that we can study the effect of the symmetry of the crystalline facets without having an explicit solid-vacuum interface.

2.4. Derivation of Voltage Curves. In a two-phase reaction between Li_xM and Li_yM, the lithiation/delithiation voltage relative to Li/Li^+ is given by the negative of the reaction free energy per Li, that is,[43]

$$V = -\{[G(Li_yM) - G(Li_xM)]/(y - x) - G(Li_{metallic})\} \quad (1)$$

where G is the Gibbs free energy and $Li_{metallic}$ refers to the bcc metallic phase of lithium. The enthalpic (pV) contribution to G is of order 10 μeV per Li at atmospheric pressure and can be safely ignored. The entropic (TS) contribution to the voltage is estimated to be systematic and of order 50 mV (see Section 3.2.1). In the following, we replace G in eq 1 with total energies (E) from DFT calculations. From E of configurations at different Li compositions, as obtained from the de/lithiation algorithm, we calculate the formation energies:

$$\Delta E(x) = [E(Li_xSi_{surface}) - xE(Li_{metallic}) - E(Si_{surface})]/N \quad (2)$$

where $E(Li_xSi_{surface})$ denotes the energy of a lithiated configuration, $E(Si_{surface})$ is the lowest-energy surface structure without Li, and N is the number of Si atoms within the slab where lithiation is allowed. Using $\Delta E(x)$, we construct the convex hull of stable phases, assume a series of two-phase reactions, and thereby derive the corresponding voltage curves from eq 1. To the extent that our simulations adequately sample configurations that are accessible by the physical system during room-temperature lithiation, the convex hulls and voltage curves correctly describe the lithiation process. In other words, our approach is valid in a constrained equilibrium in which configurations that are kinetically forbidden (e.g., most crystalline Li−Si phases) are excluded. In addition, de/lithiation reactions do not necessarily proceed strictly by two-phase reactions, especially if energies of intermediate phases do not deviate significantly from the convex hull.[44] Therefore, the voltage

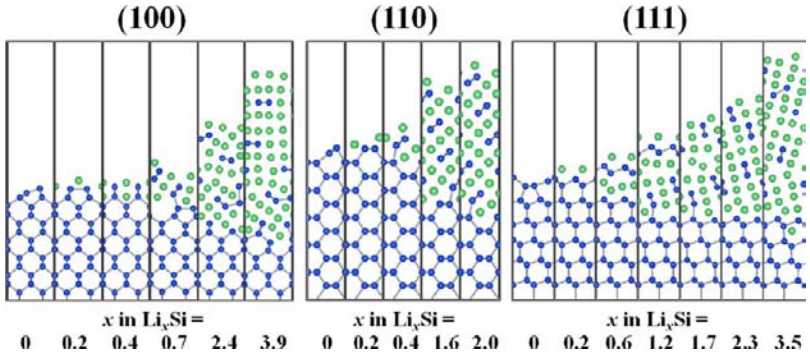

Figure 3. Configurations of the Si (100), (110), and (111) surfaces at various stages of lithium insertion for the 2-Si-per-layer models. The larger (green) spheres represent Li atoms, and smaller (blue) spheres represent Si atoms. The bottom of the surface is passivated with H atoms, and the bottom three Si layers are maintained in their bulk equilibrium configurations.

curves we derive should be viewed as approximate, and very small voltage steps should not be taken as significant.

3. RESULTS AND DISCUSSION

3.1. Atomistic Structures of Lithiated Si. *3.1.1. Lithiated Configurations.* We show, in Figure 3, configurations for the (100), (110), and (111) surfaces with two Si atoms per layer at various stages of lithiation. The most salient feature of the lithiated configurations is the progression of the amorphous−crystalline boundary as the Li content increases, indicating the two-phase nature of the reaction, which is consistent with the very low dilute solubility of Li in Si.[45] We see that the atomistic details of the amorphization process are different for the different surfaces. For the (100) and (110) surfaces, amorphization involves the breakdown into zigzag chains (appearing as dumbbells in these figures), with the chains being more ordered (aligned) for (110) than for (100). For the (111) surface, sheets of connected Si are first formed before the breakdown into zigzag chains, and some isolated Si atoms are found at high ($x \approx 3$−4) Li concentrations. We note that similar trends are observed for the lithiation of the models without a solid-vacuum interface. As shown in Figure 4, the lithiation of (110) surface with a vacuum is similar to lithiation that allows expansion in the [110] direction without an explicit vacuum; in both cases, ordered zigzag chains are formed. For both the simulations with and without a vacuum, the vertical expansion due to insertion of a given amount of Li is similar across all three surfaces. Since the volume is better defined for calculations without a vacuum, the relative volume is plotted against the degree of lithiation for these simulations in Figure 5. This result implies that the experimentally observed anisotropy is not due solely to different volumetric expansion between the different facets. We also note that the volume expansion as a function of lithium content is consistent with previous experiments[46] and simulations of lithiation of amorphous Si.[16]

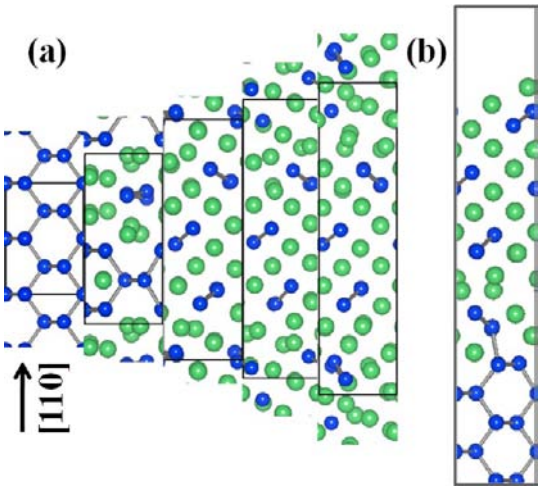

Figure 4. (a) Configurations from the lithiation algorithm for the Si (110) model without a solid-vacuum interface, consisting of four Si atoms per layer. (b) A similar configuration for the Si (110) model with a solid-vacuum interface.

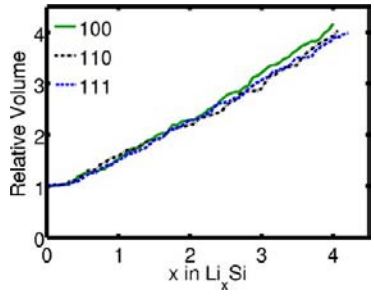

Figure 5. Volume expansion as a function of lithium content for simulations without a vacuum. Relative volume is defined as the volume of the lithiated configurations divided by the volume of unlithiated Si.

While the general trend of Si amorphization is similar, there are some variations in the process and in the details of the lithiated configurations between the 2- and 4-Si-per-layer surface models. For example, as shown in Figure 6 for Si (111), the formation of sheets at the beginning of lithiation is observed for both cell sizes, but at higher Li contents, dumbbell formation is favored in the larger cell instead of zigzag chains in the smaller ones. There is also more disorder upon lithiation in the larger cell, due to the more constrained periodicity of the smaller computational cells.

3.1.2. Radial Distribution Functions. The radial distribution function (RDF), defined as the number of neighbors of a given species per unit volume as a function of distance, gives important structural and bonding information on amorphous and crystalline solids. Experimentally, RDFs can be derived from the structure function $S(Q)$ obtained from X-ray scattering.[47] Unfortunately, the low Z-value of Li atoms renders their signal small, and hence, only Si−Si RDFs can be reliably measured.[8] From our lithiation simulations, however, we are

dx.doi.org/10.1021/ja301766z | J. Am. Chem. Soc. 2012, 134, 14362−14374

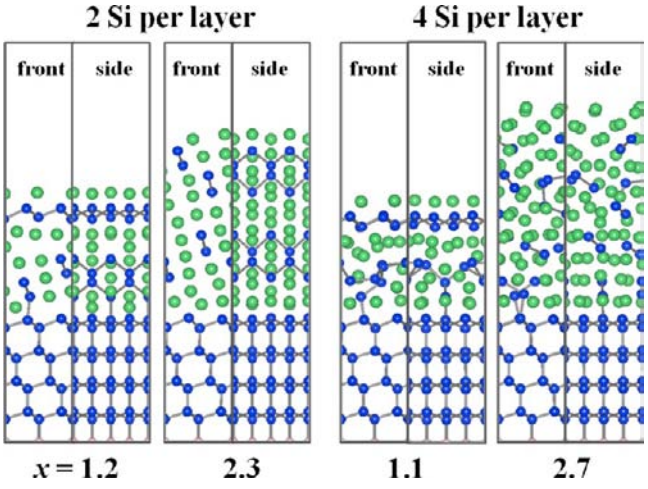

Figure 6. Comparisons of selected lithiated configurations for Si (111) 2- and 4-Si-per-layer surface models. Two different (front and side) views for each composition (x in Li_xSi) are shown. The side view for 2-Si-per-layer configurations shown represents twice the computational cell width.

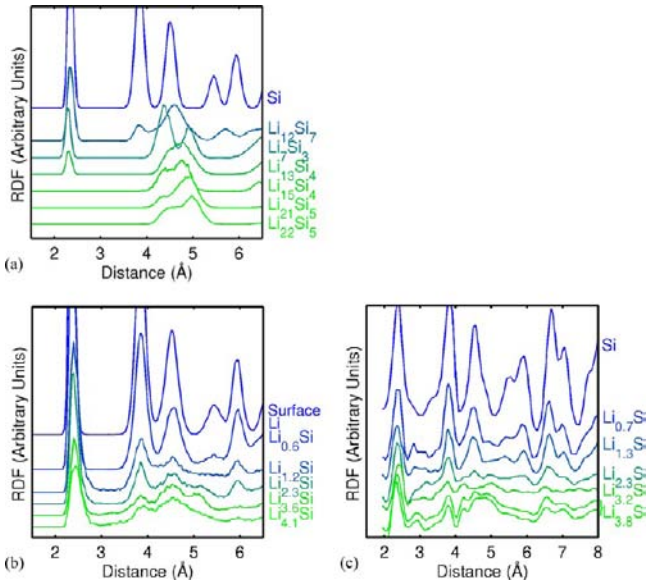

Figure 7. (a) Calculated Si−Si RDFs as a function of distance for bulk crystalline Li−Si phases. (b) Si−Si RDFs for configurations obtained by the automatic lithiation algorithm of the Si (111) surface model. A thermal distribution at 300K is obtained by a 30 ps trajectory in ab initio molecular dynamics (AIMD; see text for details). "Surface Li" refers to a configuration with Li on the surface only, but not intercalated into Si. (c) Experimental *ex situ* RDFs for polycrystalline Si at different stages of lithiation, from Figure 4 of ref 8, with major contributions from Si−Si correlations and minor contributions from Li−Si correlations. The compositions $Li_{0.7}Si$, $Li_{1.3}Si$ and $Li_{3.2}Si$ are approximate and derived from discharge voltages via Figure 3 of ref 8. It is noted in ref 8 that the feature at 2.85 Å represents contributions from Li−Si correlations. For Li−Si and Li−Li RDFs, please see Figures S1 and S2 in the Supporting Information.

able to obtain the RDFs for all species and to compare them with experimental results, where available. We can also determine RDFs from the known structures of bulk crystalline Li−Si phases (Si, $Li_{12}Si_7$,[48] Li_7Si_3,[14] $Li_{13}Si_4$,[49] $Li_{15}Si_4$,[15] $Li_{21}Si_5$,[50] and $Li_{22}Si_5$[51]) to serve as standards. The latter comparisons also allow us to gauge the structural similarities between the lithiated configurations and the bulk crystalline phases.

To obtain some level of thermal sampling for the calculated RDFs, we performed Born−Oppenheimer *ab initio* molecular dynamics (AIMD) simulations on the lithiated configurations. We take lithiated structures from the 2-Si-per-layer surface models and double them laterally to ensure that cell dimensions exceeding 5.5 Å in each direction. We use a time step of 3 fs and heat the structures to 300 K in 9 ps by velocity rescaling. The heated structures are then annealed at a constant 300 K for 30 ps using the Nosé thermostat.[52] The RDFs are obtained by extracting configurations at 0.15 ps intervals from the AIMD trajectories between 6 and 30 ps after heating is complete. The crystalline Si region where Li insertion is not allowed is excluded during the extraction of the RDFs.

The calculated Si−Si RDFs are shown in Figure 7 for the lithiated Si (111) surface as well as for bulk crystalline Li−Si phases. We also make comparisons between the calculated Si−Si RDFs and those measured in ref 8, which are predominantly from Si−Si but also contain a small contribution from Li−Si correlations. Si (111) is chosen to facilitate comparisons with experiments since it is the lowest energy surface[53] and hence is expected to be most represented in the polycrystalline samples used in the experiments. A comparison of the general features of the calculated and experimental RDFs during the lithiation process (Figure 7b and c, respectively) shows that these are similar at corresponding Li compositions, indicating that the lithiation algorithm we employ is able to capture realistic atomistic configurations during the lithiation process.

A key difference between room-temperature lithiated Si (calculated from the lithiation algorithm and measured experimentally) and crystalline Li−Si phases is the persistence, in the former, of first and second nearest-neighbor Si−Si bonds (~2.4 and 3.9 Å respectively) at high Li contents. From the Si−Si RDFs for crystalline Li−Si phases (Figure 7a), we can see that nearest-neighbor Si−Si bonds (~2.4 Å) are significantly reduced for Li_7Si_3 and $Li_{13}Si_4$ compared to pure Si and are absent for structures of higher Li content. Configurations produced from the lithiation algorithm (Figure 7b), however, show Si−Si nearest-neighbor bonds even at the highest Li concentration, which is consistent with experimental findings (Figure 7c), as well as previous modeling of lithiation of amorphous Si.[16] To a smaller extent, the same is true for the second-nearest-neighbor Si−Si bonds (~ 3.9 Å), which are formed from two Si atoms bonded tetrahedrally to the same Si atom and are also found in zigzag chains. These features are absent in all of the crystalline Li−Si phases with $x > 2$, but they persist in the calculated and experimental RDFs even for $x \sim 4$. This observation shows that it is difficult to break Si−Si dumbbells, trimers, and, to a lesser extent, zigzag chains by the insertion of Li, which may be a contributing reason for the lack of formation of crystalline Li−Si phases, which do not possess such structures, by lithiation at room temperature. The persistence of first- and second-nearest-neighbor Si−Si bonds in both computed and experimental RDFs further confirms that the lithiation algorithm is able to capture experimentally observed features of lithiation that are absent from the equilibrium crystalline Li_xSi phases.

Beyond second-nearest neighbors, between 4 and 5.5 Å, there is a broad distribution in the Si−Si RDFs for both the calculated and experimental lithiated structures. At just under 6 Å, the calculated RDFs show a peak up to $x = 2.3$, similar to the experimental data. This distance indicates a third nearest-neighbor within a zigzag chain, which is also present in a Si sheet.

dx.doi.org/10.1021/ja301766z | J. Am. Chem. Soc. 2012, 134, 14362−14374

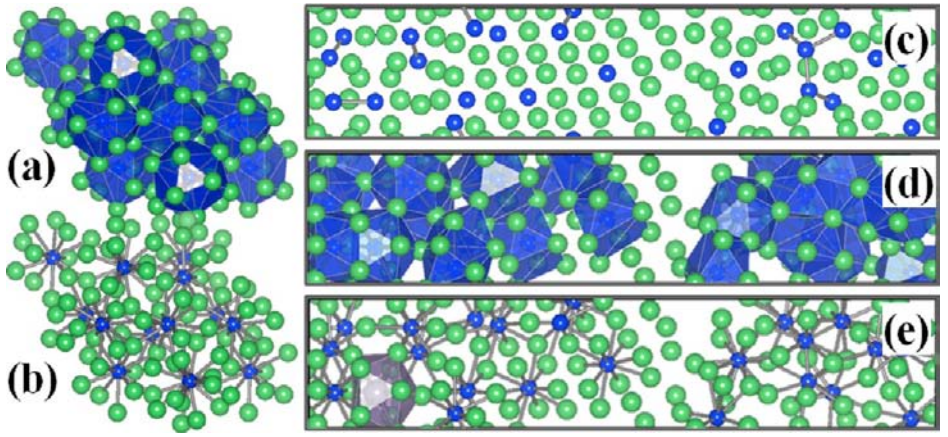

Figure 8. The $Li_{15}Si_4$ crystalline structure, with (a) and without (b) distorted icosahedra centered at the Si atoms. Larger green atoms are Li, and smaller blue atoms are Si. (c–e) The $Li_{4.125}Si$ configuration obtained from the lithiation simulation without a solid-vacuum interface and allowing expansion in the ⟨111⟩ direction. We show the same structure with Si–Si bonds (c), Si–Li bonds with polyhedra (d), and Si–Li bonds without polyhedra (e).

The disappearance of this peak beyond $x = 2.3$ shows that this is the Li concentration beyond which larger Si clusters are broken down.

The Li–Si and Li–Li RDFs from the lithiation simulation of the same Si (111) surface are shown in the Supporting Information (Figures S1 and S2). Beyond $x = 1$, the Li–Si RDFs of the lithiated configurations resemble those of $Li_{13}Si_4$, $Li_{15}Si_4$, $Li_{21}Si_5$, and $Li_{22}Si_5$, which are in turn similar to each other. For the lithiated configuration $Li_{3.6}Si$, there is a slightly closer resemblance to the $Li_{15}Si_4$ phase based on the multipeak structure of the Li–Si correlations in the 6–8 Å range. The Li–Li RDFs of the lithiated configurations for $x > 1$ resemble those of Li_7Si_3, $Li_{13}Si_4$ and $Li_{15}Si_4$, and are distinctly unlike those of $Li_{21}Si_5$ or $Li_{22}Si_5$, based on the presence/absence of peaks between 5 and 6 Å, and between 7 and 8 Å. The results indicate that the Li local environments do not undergo significant changes after the initial stage of lithiation and are most similar to those in the crystalline phases $Li_{13}Si_4$ and $Li_{15}Si_4$. To experimentally confirm this prediction, an approach that is more sensitive to Li local environments than current techniques, such as nonresonant inelastic scattering,[54] could be employed.

3.1.3. Formation of $Li_{15}Si_4$. As discussed in the Introduction, one of the intriguing features of the lithiation process of crystalline Si is the formation of the $Li_{15}Si_4$ phase after significant lithiation and amorphization has occurred. The structure of $Li_{15}Si_4$ has been characterized by XRD[21] and studied by DFT calculations.[23,24] It has the $Cu_{15}Si_4$ prototype, and the space group is $I\bar{4}3d$. There are no Si–Si nearest-neighbor bonds within the structure, and each Si atom is bonded to 12 Li atoms with bond lengths of 2.6–2.9 Å, forming distorted icosahedra (Figure 8, a and b). From the discussion of radial distribution functions in Section 3.1.2, we saw that nearest-neighbor Si–Si bonds persist at the end of lithiation in both the lithiation algorithm and experimental measurements, which means that the formation of $Li_{15}Si_4$ is incomplete. We note, in passing, that the persistence of nearest-neighbor Si–Si bonds may also explain why, from both our simulations and experiments, lithiation stops at a stoichiometry less than the maximum 4.2 or 4.4 Li per Si allowed in the crystalline Li–Si phases ($Li_{21}Si_5$ or $Li_{22}Si_5$), since residual unbroken Si–Si pairs limit the maximum number of Li atoms that can be bonded to Si.

Despite the incomplete formation of $Li_{15}Si_4$, some of the features of this phase are apparent in configurations obtained by the lithiation algorithm. In the lithiation simulation of a Si cell with no solid-vacuum interface which is allowed to expand only in the ⟨111⟩ direction, the limit of lithiation is reached with $Li_{4.1}Si$ at approximately 0 V. As shown in Figure 8c, the lithiated configuration at this composition shows some nearest-neighbor Si–Si bonds which are not found in $Li_{15}Si_4$. Nonetheless, from Figure 8d, we see that there are a few isolated Si atoms bonded with approximately 12 Li atoms, forming distorted icosahedra, an example of which is shown in Figure 8e. The formation of isolated Si atoms near 0 V is also found experimentally as a second process subsequent to the formation of small Si clusters during lithiation using NMR and X-ray PDF analysis.[8]

Further similarities between this lithiated configuration and $Li_{15}Si_4$ can be found by comparing the Li–Li, Li–Si, and Si–Si RDFs of the two structures obtained using AIMD, as shown in Figure 9. Apart from the presence of Si–Si bonds at ~2.4 Å in

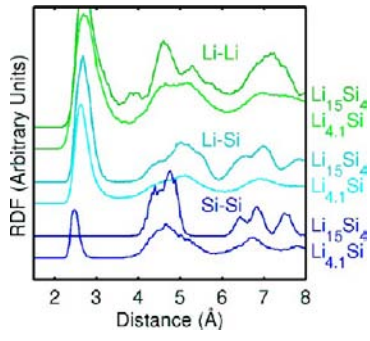

Figure 9. Li–Li, Li–Si, and Si–Si RDFs of the $Li_{15}Si_4$ crystalline phase (higher, darker line in each set) compared with the $Li_{4.125}Si$ lithiated configuration from the Si ⟨111⟩ simulation cell without a solid-vacuum interface (lower, lighter line in each set). Both structures are heated to and annealed at 300 K (see text for details).

the lithiated configuration, which we have remarked upon (Section 3.1.2), the (Si–Si, Li–Si, and Li–Li) RDFs of the lithiated configuration are very analogous to those of $Li_{15}Si_4$, although some similarities to $Li_{13}Si_4$ are also apparent. Inspection of the Li–Li RDFs (Figure S2) also shows that the peak between 7 and 8 Å found in the $Li_{4.1}Si$ simulated configuration is found for $Li_{15}Si_4$ but not $Li_{13}Si_4$. The similarities in the RDFs suggest that the $Li_{4.1}Si$ configuration

dx.doi.org/10.1021/ja301766z | J. Am. Chem. Soc. 2012, 134, 14362–14374

from the simulation algorithm is consistent with a partial formation of a $Li_{15}Si_4$-like phase.

3.2. Lithiation Voltages and Robustness of Lithiation Algorithm. *3.2.1. Convex Hulls and Voltage Profiles.* For the (100), (110), and (111) surface models with two Si atoms per layer and an explicit vacuum, we calculate the formation energies of all configurations at each step of the lithiation routine according to eq 2. The formation energies, the associated convex hulls, and the corresponding voltage curves are determined as discussed in Section 2.4 and shown in Figure 10. The value of x in Li_xSi is the number of Li atoms divided by the number of Si atoms in the slab region where lithiation is allowed. The high voltage step at small x, at 0.8−1.0 V, is due to a single monolayer of adsorbed surface Li. A comparison of the voltage curves for the three different surfaces is shown in Figure 11a. We see that (110) shows a higher voltage plateau than do the other two surfaces. As we will discuss in Section 3.3, this difference in lithiation voltages can explain the drastic lithiation anisotropy observed experimentally in microstructures and nanowires.

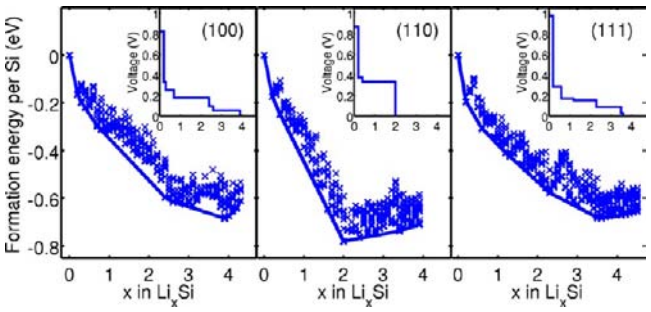

Figure 10. Convex hulls and first lithiation voltage profiles (insets) for the (100), (110), and (111) surfaces, constructed from energies produced from the lithiation algorithm. Energies of all calculated configurations at each composition are shown by crosses.

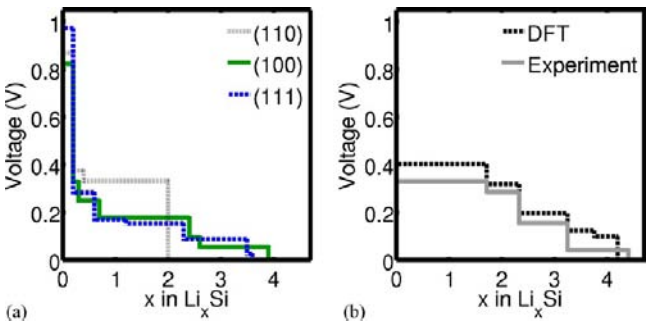

Figure 11. (a) Comparison of calculated voltage curves from the lithiation of Si (100), (110), and (111) surface models with two Si atoms per layer. (b) Calculated (DFT) vs high-temperature (400 °C) experimental[1] voltage curves for bulk crystalline Li_xSi phases.

The formation energies for the bulk Li_xSi phases (Si, $Li_{12}Si_7$,[48] Li_7Si_3,[14] $Li_{13}Si_4$,[49] $Li_{15}Si_4$,[15] and $Li_{21}Si_5$[50]) are also computed, and the corresponding voltage curve is shown in Figure 11b, together with the high temperature experimental voltage curve[1] for comparison. We see that there is generally very good agreement between DFT and experiment, although DFT voltages are systematically higher than experimental voltages by an average of 58 mV. The discrepancy, similar to the values Chevrier et al. reported,[14] is due either to DFT errors, or the neglect of the entropic contribution to the free energy in the computations, since the magnitude of the difference is consistent with the value of k_BT for the high temperature experiment (59 meV at 400 °C) and similar to measured entropic contributions to voltages (~0.05−0.1 V) in the analogous Li−Ge system.[55] However, since the error is systematic, computed differences between different surface orientations should not be significantly affected.

3.2.2. Effects of Variations in the Cell Size and Lithiation Algorithm. We have performed extensive tests on the effects of the cell size and variations in the lithiation algorithm on the derived voltage curves. As discussed in more detail in Supporting Information Section SI.2.1, the 2- and 4-Si-atom-per-layer models are found to produce voltage curves that are similar. Variations in the lithiation algorithm are discussed in Supporting Information Section SI.2.2. These variations include changing the value of the parameter d_{min}, restricting Li insertion to the Si layer immediately below the region of the Si slab that has already been lithiated, and choosing two lowest-energy configurations (instead of just one) at each step to continue the lithiation algorithm. None of these variations produce significant differences in the lithiation voltages, indicating that the voltage profiles resulting from our simulations are robust.

3.2.3. Effects of the Presence of Solid-Vacuum Interface. The voltage curves from lithiation simulations which do not contain a solid-vacuum interface, yet capture some of the geometrical effects of lithiating crystalline Si in specific orientations (e.g., formation of zigzag chains for (110), as shown in Figure 4), are shown in Figure 12. We see that, apart from the absence of a high (>0.8 V) voltage plateau arising from surface lithiation in calculations without a vacuum, the voltage curves are not significantly affected by the inclusion of a solid-vacuum interface. In particular, the lithiation voltage remains higher for expansion along the ⟨110⟩ direction compared to the other two directions. Our results thus strongly suggest that it is the geometrical constraints of the various Si facets, rather than the explicit presence of a surface, that determines many of the lithiation features, including the calculated anisotropy between the (110) facet and the other facets. This conclusion further suggests that Si surfaces that are terminated by passivating hydrogen, thin oxide layers, or other electrolyte decomposition products in the solid-electrolye interphase, as is the case in realistic Si anodes, will show similar lithiation energetics.

3.2.4. Thermal Stability of Lithiated Configurations. To check the stability of the lithiated configurations produced by the insertion algorithm against other thermally accessible structures, we perform AIMD simulations on structures from the lithiation simulations, in 2- and 4-Si-per-layer cells (Figure 10 and Figure S3). AIMD simulations are performed as described in Section 3.1.2. The configurations after annealing are quenched to 0 K with local structural relaxations, and the relaxed energies are compared with the original energies before heating and annealing. The results are shown in Figure 13. We see that the energies of the structures obtained by the lithiation algorithm are not significantly changed after AIMD and subsequent relaxation, indicating that structures obtained from the lithiation algorithm are locally stable. While in some cases, annealing and relaxation leads to lower-energy structures than those found by the lithiation algorithm, the effect on the lithiation voltages is less than 0.05 V for all three surfaces at all Li concentrations considered.

3.3. Lithiation Anisotropy. *3.3.1. Atomistic Mechanism of Anisotropic Lithiation.* We have established from Sections 3.1 and 3.2 that, based solely on the tendency of Li to occupy

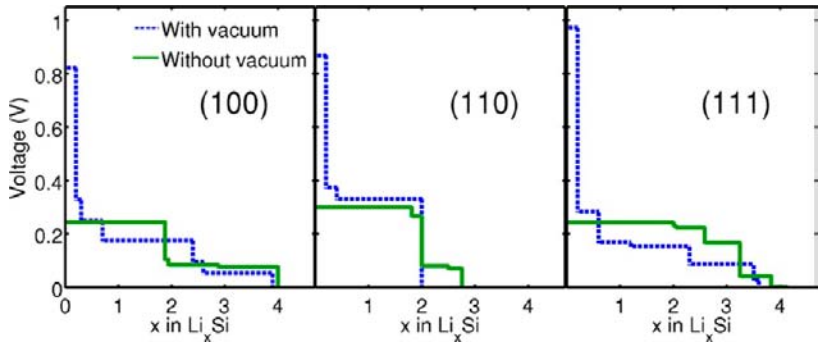

Figure 12. Comparison of voltage profiles for surface cells with vacuum layers (blue dashed lines) vs periodic cells without vacuum layers (green solid lines). See text for details.

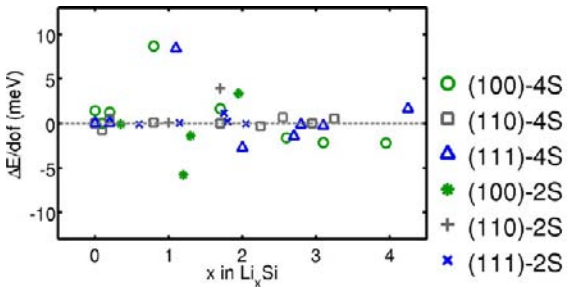

Figure 13. Change in total energies per degree of freedom (dof, equal to three times the number of atoms) after heating to and annealing at 300 K with AIMD and subsequent relaxation, compared to the original relaxed structures from the lithiation algorithm.

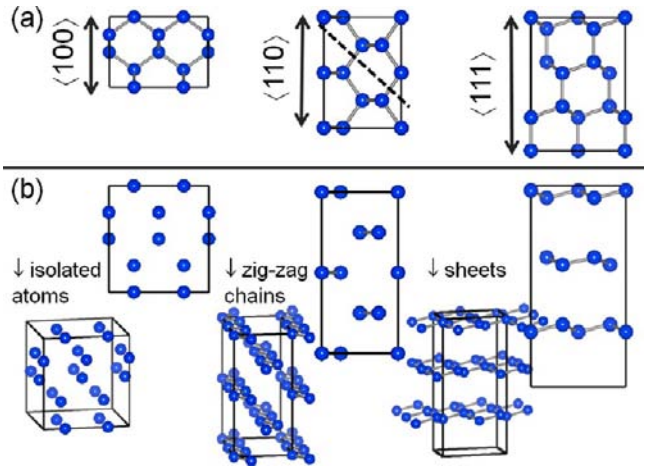

Figure 14. (a) Crystalline Si along the ⟨100⟩, ⟨110⟩, and ⟨111⟩ crystallographic orientations; (b) the configurations in (a) strained along the three directions by 50%, side and perspective views. Straining along the ⟨100⟩, ⟨110⟩, and ⟨111⟩ directions forms isolated atoms, zigzag chains, and sheets, respectively. The dashed line on the ⟨110⟩ cell denotes a (111) plane.

interstitial spaces and the geometric constraints of the different Si surface crystallographic orientations, significant differences in lithiated configurations and voltages are produced. Further understanding of the atomistic mechanism for these differences is desirable. Since one of the major components of lithiation is the vast expansion of the Si lattice, we would like to isolate the effects of straining the Si structure from chemical effects of Li−Si bonding. To this end, we consider expansions of the native Si crystal along the three different orientations. Periodic bulk Si cells, the same as those used for lithiation simulations without a solid-vacuum interface, are strained along the ⟨100⟩, ⟨110⟩, and ⟨111⟩ orientations in 5% steps, and the atoms are relaxed at each step. Figure 14 shows the resultant side and perspective views when the cells are elongated by 50% of the original length along these orientations. The bonds shown connect Si−Si atoms that are at most 2.6 Å apart (the first nearest neighbor distance is 2.37 Å within GGA-PBE). Since Si (111) is the lowest-energy surface,[53] cleaving along (111) planes requires the least energy; so it is unsurprising that straining along the ⟨111⟩ direction results in sheets of connected Si atoms. Straining along the ⟨110⟩ direction also breaks apart Si along (111) planes (dashed line), forming zigzag chains of Si atoms. Straining along the ⟨100⟩ direction, on the other hand, produces isolated Si atoms. Such differences mirror the orientation-dependence in configurations of the lithiated structures, with the lithiation of (100) surface producing more amorphous configurations, (110) surfaces producing long zigzag chains and/or dumbbells, and (111) surfaces producing, at least initially, sheets of Si atoms (Figure 3).

The above atomistic picture of anisotropy in the lithiation mechanism is also consistent with results of Raman spectroscopy. When Goldman et al.[31] studied the lithiation of Si wafers in different orientations by monitoring the strength of the 520 cm^{-1} phonon mode, they found that the Si(111) wafers experienced a slower decay, compared to (110) and (100) wafers, of the phonon mode with voltage after the onset of lithiation. Since the disappearance of the phonon mode indicates the destruction of long-range correlation in the Si lattice, the formation of Si sheets (Figure 14) as an intermediate step during lithiation of Si (111) should help maintain long-range correlations and contribute to the slower decay of the phonon mode.

It is also instructive to consider the strain energies for expansion in different directions, as shown in Figure 15. For both the ⟨110⟩ and ⟨111⟩ directions, the energy change saturates at 30−70% strain (z/z_0 = 1.3−1.7). This shows that upon the complete separation of Si sheets for ⟨111⟩ and the separation of zigzag chains for ⟨110⟩, further elongation of the cell does not contribute to significant energy changes. In contrast, the energy continues to increase with elongation in the ⟨100⟩ direction up to 200% strain (z/z_0 = 3). The energetic penalty for straining along the ⟨110⟩ direction is larger than that along the ⟨111⟩ direction; nevertheless, the lithiation voltages are higher in the former direction as compared to the latter. The lithiation voltage can be thought of as a sum of three terms: negative terms corresponding to the energetic penalty from straining or breaking Si−Si and Li−Li bonds, and a positive term corresponding to energy gain from forming Li−Si

dx.doi.org/10.1021/ja301766z | J. Am. Chem. Soc. 2012, 134, 14362−14374

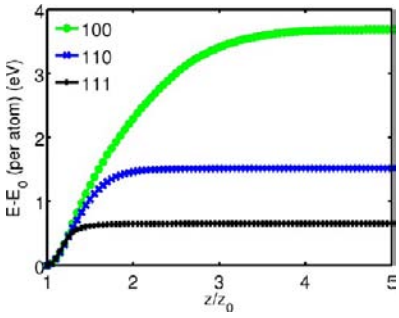

Figure 15. The energy change per atom $(E - E_0)$ as a function of strain z/z_0 (the ratio of strained cell length to original cell length) for elongation along the ⟨100⟩, ⟨110⟩, and ⟨111⟩ crystallographic orientations for bulk Si.

bonds. The difference in the orders of strain energies and voltages between ⟨110⟩ and ⟨111⟩ points to stronger binding of Li with zigzag chains of Si as compared to the Si sheets or derivatives thereof.

To delineate the contributions of strain energies and Li−Si bonding energies, we calculate, separately, the total energies of the Li atoms and the Si/H atoms in the lithiated (100), (110), and (111) surfaces, frozen at the positions after lithiation. The Li strain energy (ΔE_{Li}) is defined as the difference between the total energies of the Li atoms and that of an equal number of Li atoms in bulk metallic Li. The Si strain energy (ΔE_{Si}) is defined as the difference between the Si surfaces distorted due to Li insertion and the original Si surfaces. The Li−Si bonding energy (ΔE_{Li-Si}) is defined as the energy difference between the combined Li−Si calculation and the Li and Si strain energies. The sum ($\Delta E_{Li} + \Delta E_{Si} + \Delta E_{Li-Si}$) gives the formation energy. The three energies are shown in Figure 16. We can see that, while the strain energy penalty for (110) is large, the magnitude of the Li−Si bonding energy is also large. The net result is more favorable overall formation energies and, hence, a higher lithiation voltage plateau, for the (110) surface, at $x \sim 2$.

3.3.2. From Surface Lithiation Voltages to Anisotropic Expansion. Although we have demonstrated differences in lithiation voltages for the various crystal facets, it is not immediately apparent from these results alone that the expansion of Si electrodes during lithiation should be strongly anisotropic. Indeed, one might expect that, since the diffusion is isotropic within bulk Si, the surface effects will not penetrate to any appreciable depth. However, we argue that the thermodynamic favorability of Li insertion in a particular surface [(110) in this case] is a sufficient condition for the observed anisotropy. To illustrate, we solve the unsteady-state diffusion equation for a rectangular pillar with the boundary conditions that the side surface has a larger solubility for Li than the top surface (e.g., by a factor of 10). The bottom surface is maintained at zero flux of Li atoms. Even with a scalar diffusion coefficient (isotropic diffusion), the resultant Li concentration profiles, as shown in Figure 17a, demonstrate a large anisotropy. The concentration profiles, together with the expected expansion of the lithiated region, bear a strong resemblance to the shape of lithiated Si microstructures (Figure 17b). The results of Figure 17 demonstrate that we can explain the experimentally observed lithiation anisotropy using only anisotropy in thermodynamics, manifested as a difference in lithiation voltages for different directions, without requiring anisotropic diffusion behavior.

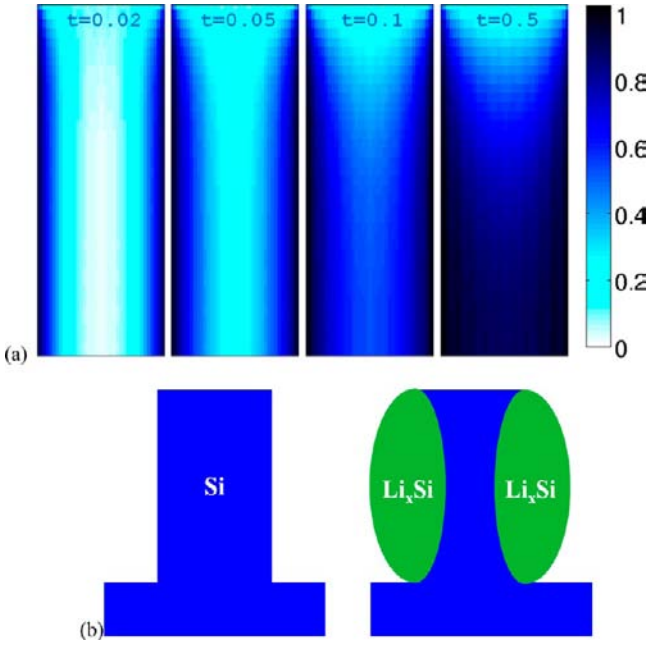

Figure 17. (a) Lithium concentration profiles for a Si microstructured column that allows higher solubility of Li on the side wall ((110)) than on the top wall ((111)), as a function of time. The time t is given in units of the diffusion time, A^2/D, where A is a characteristic length scale of the structure and D is the diffusion constant. A scalar diffusion coefficient (isotropic diffusion) is assumed. (b) Schematic figure showing the profile of a Si microcolumn before and after lithiation, adapted from Figure 3 of ref 31.

3.3.3. The Role of Diffusion Anisotropy. The anisotropy in the lithiation of Si micro- and nanostructures has been previously attributed to the difference in diffusion rates in

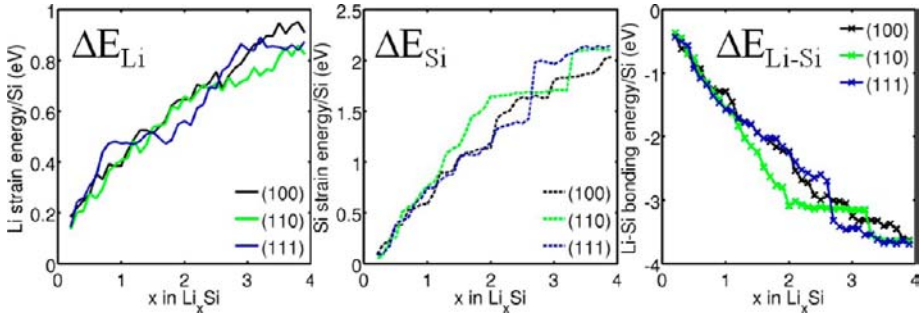

Figure 16. Li strain energies, Si strain energies, and Li−Si bonding energies calculated from separating the Li and Si atoms in the lithiated configurations. See text for definitions of strain and bonding energies.

dx.doi.org/10.1021/ja301766z | J. Am. Chem. Soc. 2012, 134, 14362−14374

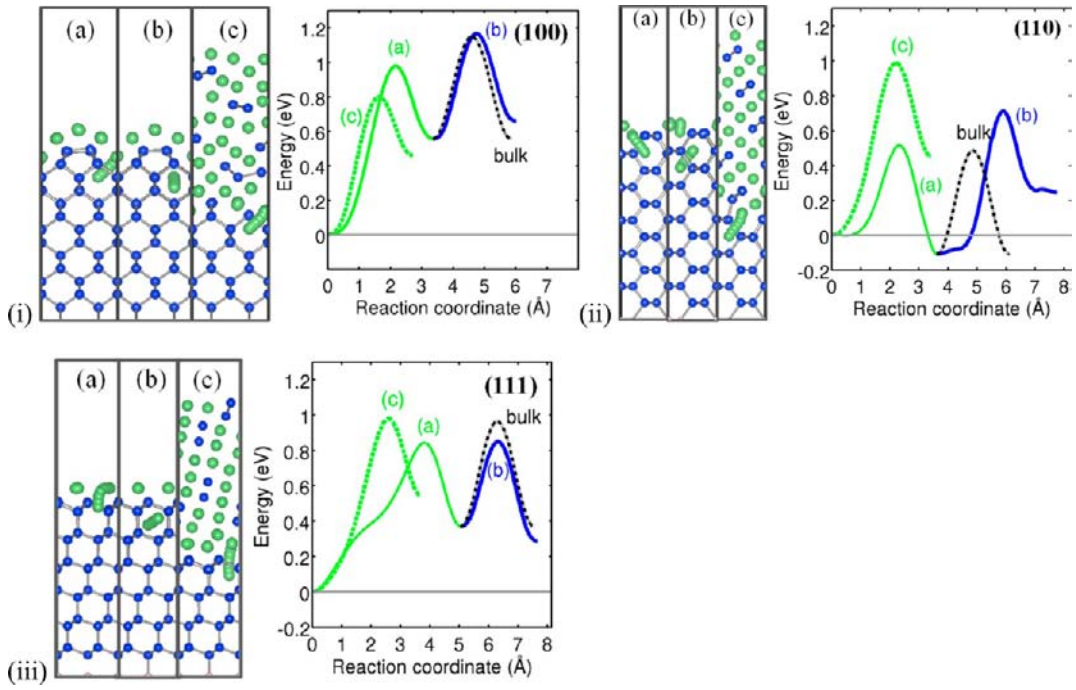

Figure 18. Diffusion barriers and paths for Li in lithiated Si (i) (100), (ii) (110), and (iii) (111) surfaces. (a) From the lowest surface site to the first subsurface site for one monolayer (1 ML) of adsorbed Li; (b) from the first subsurface site to the nearest lower subsurface site for 1 ML Li; (c) from the bottom of a layer of lithiated Si to the first interstitial site in the unlithiated region. The bulk diffusion barrier is shown with dashed lines for comparison.

different directions.[31,32] To investigate the role of diffusion rates, we perform climbing image nudged elastic band (NEB)[56] calculations of Li diffusion barriers for different lithiated structures, using the VASP Transition State Tools (VTST[57]) package. Within bulk crystalline Si, Li atoms jump between adjacent interstitial sites with a diffusion barrier of 0.65 eV.[58] The diffusion coefficient depends on the jump distance as well as the diffusion barrier. While the projection of the diffusion path between adjacent tetrahedral sites along the ⟨100⟩, ⟨110⟩, and ⟨111⟩ directions gives different jump distances, the differences are small so that the diffusion coefficients are comparable. Moreover, it is known that the diffusion of Li in Li_xSi is faster than in Si.[1] Since diffusion within bulk Si is not strongly orientation-dependent and diffusion in Li_xSi is rapid, the rate-limiting diffusion barriers that may be different based on orientations are at (a) or near (b) the Si surfaces or at interfaces between lithiated and unlithiated regions (c). For a clean surface, a single monolayer of Li coverage occurs at the highest voltage, so we calculate the diffusion barriers for Li through the one-monolayer-covered surfaces of different orientations, and the NEB path and energies are shown in Figure 18a. The diffusion barrier from first subsurface to second subsurface layer is also calculated (Figure 18b). There are many possible configurations for interfaces between the lithiated and unlithiated regions, and we take for each surface an example of a highly lithiated configuration found from the lithiation algorithm (Figure 18c). An exhaustive sampling of diffusion barriers through all lithiated-unlithiated boundaries is currently computationally prohibitive.

We see that for surface-to-subsurface diffusion with a monolayer coverage ((a) in Figure 18i–iii), the (110) direction shows a lower diffusion barrier than do the other directions. For first to second subsurface layer diffusion (b), and through the chosen lithiated-unlithiated boundaries (c), however, the diffusion barriers in the three orientations are similar. Therefore, any diffusion anisotropy should not be drastic nor persist beyond the first atomic layer. In structures of size exceeding several nanometers, we conclude that diffusional anisotropy does not play a significant role in the observed lithiation anisotropy. As discussed in Section 3.3.1 the slower decay of the 520 cm^{-1} phonon mode for (111) wafers compared to the other facets, which was cited as the primary evidence for diffusional anisotropy in ref 31, can be explained by the tendency for layer-by-layer exfoliation of crystalline Si when strained along the ⟨111⟩ direction.

3.4. Delithiation and Relithiation. *3.4.1. Hysteresis in Lithiation and Delithiation Processes.* To this point, all calculations have been performed for lithiation of Si. We next turn to the *delithiation* of the Li_xSi cells. The delithiation procedures, as described in Section 2.3, are carried out starting from the highest Li content configuration on the convex hull for each Si surface orientation. The resulting convex hulls and voltage curves are shown in Figure 19. The formation energies

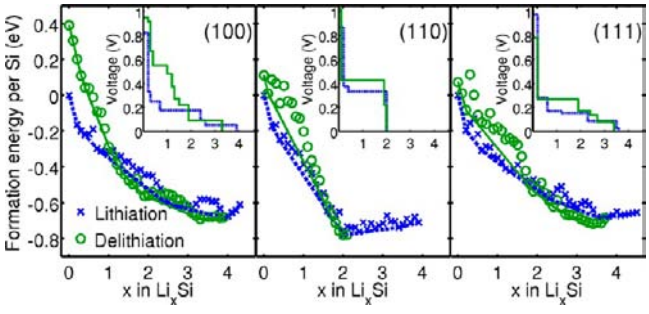

Figure 19. Comparisons between the convex hulls and voltages for first lithiation and first delithiation processes. For clarity, only the lowest-energy configuration for each composition is shown. The formation energies are calculated relative to the lowest-energy unlithiated Si surface models.

dx.doi.org/10.1021/ja301766z | J. Am. Chem. Soc. 2012, 134, 14362–14374

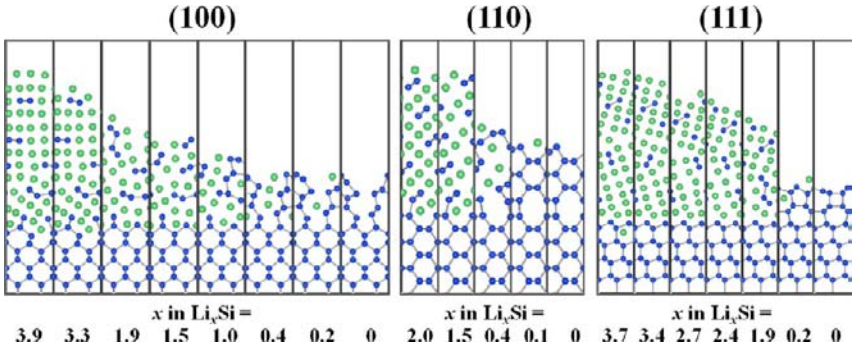

Figure 20. Configurations of the lithiated Si (100), (110), and (111) surfaces during different stages of delithiation. The configurations shown lie on the convex hull of formation energies for all configurations sampled during the delithiation simulation.

for both the lithiation and delithiation processes are calculated relative to the lowest-energy unlithiated (clean) Si surfaces for each orientation. Because the lithiation and delithiation process is accompanied by the amorphization of Si, one expects the fully delithiated structures to have higher energies than the original unlithiated structures, and indeed this is what we observe. The energy difference is approximately 0.1 to 0.4 eV per Si, in reasonable agreement with the energy difference between amorphous and crystalline bulk Si, measured to be 0.1 eV/atom[59] and calculated to be 0.2−0.3 eV/atom.[60−62]

We note that in all three orientations, the average delithiation voltages are higher than the average lithiation voltages, consistent with experimental observations.[8] The hysteresis loop on the first lithiation−delithiation cycle represents an energy loss that goes into the amorphous−crystalline energy difference, a loss that is irreversible without restoring the crystallinity upon delithiation. The lithiation algorithm is able to capture this hysteresis because the relaxations upon each Li insertion destroy the Si crystalline order, and the configurational space for amorphous Si is substantially larger than that of crystalline Si. The relaxations upon Li removal during delithiation are therefore more statistically likely to reach an amorphous configuration than to return to the original crystalline state. The size of the hysteresis loop correlates with the change in energy of the fully delithiated structure compared to the pristine, crystalline, unlithiated structure, with (100) having larger hysteresis than (110) or (111). The higher energy of the delithiated (100) structure, in turn, indicates either a higher degree of amorphization or less restoration of Si−Si crystalline order upon Li removal. A variety of factors may affect the degree of restoration of crystalline order, such as the rate of delithiation, the existence of crystalline Si beneath the lithiated layer, or the use of nanostructures.[63] Other contributions to hysteresis not captured in our simulations include: (1) effects of the crystallization of $Li_{15}Si_4$ on the hysteresis,[22] due to the incomplete formation of $Li_{15}Si_4$ as discussed in Section 3.1.3; (2) diffusion overpotential,[17] since diffusion barriers are not taken into consideration; and (3) hysteresis due to barriers involved in bond breaking,[17] since relaxed energies are used. From the delithiation simulation, it appears that there can be anisotropy in the delithiation hysteresis, although we caution that the delithiation voltages may be more sensitive to the details of the algorithm than the lithiation voltages, as discussed below.

3.4.2. Delithiated Configurations. The configurations at various stages of the delithiation simulations for the different surface orientations are shown in Figure 20. We see that at the end of delithiation, an amorphous Si layer remains for all three surfaces, although the degree of amorphization appears to be smaller for (110) and (111), consistent with the smaller size of the hysteresis loop for these two surfaces. AIMD simulations of these configurations show that most are stable, at least within the computationally accessible time scales, against thermally accessible configurations, meaning that after heating, room-temperature annealing, and relaxation, the total energies do not change appreciably (<10 meV per degree of freedom). An exception is the fully delithiated configuration for the (100) surface, which shows a larger (60 meV per degree of freedom) decrease in energy. Tests of variations in the delithiation algorithm (Supporting Information Section SI.2.3) also show that the size of the hysteresis loop is more sensitive to the order in which the Li atoms are removed for the (100) surface than for (110) or (111), consistent with the larger changes seen upon heating, annealing, and relaxation.

3.4.3. Relithiation of Amorphized Delithiated Silicon Surfaces. Relithiation of the fully delithiated structures is performed using the same lithiation algorithm, and the resultant convex hulls and voltage curves are shown in Figure 21.

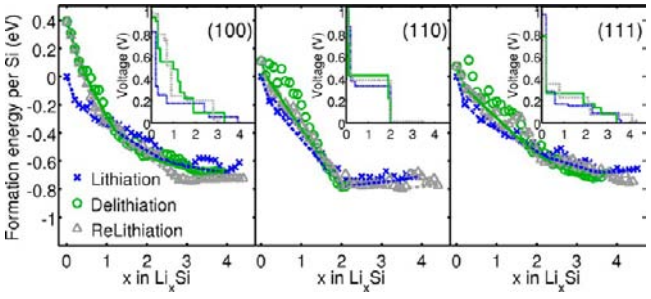

Figure 21. Comparisons between the convex hulls and voltages for first lithiation, first delithiation, and second lithiation processes. All Li insertion/removal sites are sampled for the de/re/lithiation process. Only the lowest-energy configuration for each composition is shown. The formation energies are calculated relative to the lowest energy unlithiated Si surface models.

The first lithiation and delithiation curves are also shown for comparison. We see that there is a small amount of hysteresis between the first delithiation and relithiation, although the magnitude is clearly smaller than that between the first lithiation and delithiation. We note that, given the uncertainties in the delithiation algorithm, described in section 3.4.2 above, it may be that the hysteresis between the delithiation and relithiation curves is within the error bars of the method. In any case, we expect the hysteresis in subsequent cycles to be smaller than between first lithiation and delithiation, because the first

dx.doi.org/10.1021/ja301766z | J. Am. Chem. Soc. 2012, 134, 14362−14374

delithiation and relithiation both sample amorphous structures, for which the energy differences are smaller compared to those between amorphous and crystalline structures. Since the second-cycle lithiation voltages are higher than those in the first cycle, second lithiation will preferentially occur in the region lithiated in the first cycle. That the second cycle lithiation voltages are anisotropic suggests that as long as Si micro and nano structures are not fully lithiated, and a crystalline core is preserved, anisotropy may be preserved in further lithiation cycles. The effects of surface species such as H and O on the persistence of anisotropy remain to be investigated.

4. CONCLUSIONS

To understand the myriad intriguing phenomena related to the electrochemical lithiation of crystalline Si, we have developed a physically motivated, history-dependent first principles technique to simulate the process of Li insertion and removal from faceted crystalline Si. The simulations give a detailed atomistic picture of the structural and energetic features of the lithiation process, including the crystalline−amorphous transitions that Si undergoes during lithiation, the voltages associated with lithiation of the (100), (110), and (111) surfaces, and hysteresis that is observed during subsequent delithiation/relithiation cycles. A detailed structural analysis of the lithiated configurations of the various facets demonstrates that, while lithiation clearly disrupts the ordering of the Si atoms and leads to partial amorphization of the surfaces, a variety of multiatom Si structural motifs persist. For the (111) surface (expanding along the ⟨111⟩ direction), the Si crystal is first broken apart into layers, while for (110) and (100) surfaces, zigzag chains form. The predicted differences in how Si is broken apart are consistent with the rate of amorphization for wafers of different orientations as measured by monitoring the rate of decay of the 520 cm^{-1} phonon mode.[31] These results provide useful interpretations of the features observed in experimentally-determined radial distribution functions and strongly suggest that it is energetically unfavorable to fully break apart Si clusters and chains during room-temperature lithiation processes. This conclusion, in turn, also speaks to the difficulty of forming crystalline Li_xSi phases at high lithium contents; we see only hints of the formation of structures that resemble the $Li_{15}Si_4$ phase, which crystallizes at the end of lithiation.

From the DFT-determined energetics of the structures described above, we have further derived voltage curves for lithiation and delithiation of the (100), (110), and (111) surfaces. Insertion of Li is more energetically favorable (occurs at a higher voltage) in the (110), as opposed in the (111) and (100), surfaces. Lithiation patterns of Si unit cells that impose the same planar symmetry as the (111), (110), and (100) surfaces, but do not contain an explicit vacuum, are very similar to the corresponding patterns for the vacuum-containing surfaces, demonstrating that it is the inherent symmetry of the Si facets, rather than the explicit presence of a Si/vacuum interface, that produces the anisotropy. The different energetics of the different surfaces, in turn, are traced to a delicate interplay of strain-induced distortion of the Si lattices and attractive interactions between Li and Si atoms.

The differences in lithiation thermodynamics of the various Si surfaces imply that lithium will generally be present at higher concentrations near the (110) surfaces and suggest that significant lithiation anisotropy would be observed in Si micro or nanostructures that exhibit different crystalline facets. In fact, an analytical solution to a standard diffusion equation shows that such anisotropy in thermodynamics can cause anisotropic expansion of microstructured electrodes, even if the diffusion tensor itself is isotropic, thus providing a compact explanation for numerous recent experimental results on micro- and nanostructured electrodes. The thermodynamic explanation circumvents the difficulties in using diffusion to explain the lithiation anisotropy, since beyond a few atomic layers, the diffusion tensor within the Si crystal obeys the cubic symmetry of the lattice.

Finally, we have also simulated delithiation of the different Li_xSi surfaces and have determined that delithiation generally occurs at higher voltages than does the initial lithiation. This hysteresis, which is also observed experimentally, results from the energy difference between the delithiated amorphous Si and the original crystalline Si, and the size of the resulting hysteresis loop depends on the degree to which crystallinity is restored upon delithiation. We demonstrate that subsequent relithiation shows a smaller hysteresis and persistent anisotropy, implying that lithiation anisotropy should persist in subsequent cycles.

The atomic-scale structural and energetic insights of Si lithiation derived from the present DFT calculations provide a new perspective on the significant anisotropy that has recently been observed during lithiation and delithiation of Si micro- and nanostructres. These insights provide an important basis for future studies of the effects of SEI formation and nanostructuring on the dynamics of Si electrodes in lithium ion batteries and may, ultimately, facilitate the design of improved electrode architectures for these critical energy storage devices.

■ ASSOCIATED CONTENT

Ⓢ Supporting Information

Details on the selection of Li insertion sites in the lithiation algorithm; Li−Li and Li−Si radial distribution functions; tests of robustness of lithiation and delithiation algorithms, including the effects of the surface cell size, variations in the lithiation algorithm, and variations in the delithiation algorithm. This material is available free of charge via the Internet at http://pubs.acs.org.

■ AUTHOR INFORMATION

Corresponding Author

mchan@anl.gov; jgreeley@anl.gov

Notes

The authors declare no competing financial interest.

■ ACKNOWLEDGMENTS

We are grateful to Vincent Chevrier, Brandon Long, Andrew Gewirth, Jason Goldman and Ralph Nuzzo for helpful discussions. This work was supported by the Center for Electrical Energy Storage (CEES): Tailored Interfaces, an Energy Frontier Research Center at Argonne National Laboratory, Northwestern University, and University of Illinois at Urbana—Champaign, funded by the U.S. Department of Energy, Office of Science, Office of Basic Energy Sciences. Use of the Center for Nanoscale Materials was supported by the U.S. Department of Energy, Office of Science, Office of Basic Energy Sciences, under contract No. DE-AC02-06CH11357. The authors also acknowledge grants of computer time from EMSL, a national scientific user facility located at Pacific Northwest National Laboratory, and the Fusion cluster in the

Laboratory Computing Resource Center at Argonne National Laboratory.

REFERENCES

(1) Wen, C. J.; Huggins, R. A. *J. Solid State Chem.* **1981**, *37*, 271.
(2) Beaulieu, L. Y.; Hatchard, T. D.; Bonakdarpour, A.; Fleischauer, M. D.; Dahn, J. R. *J. Electrochem. Soc.* **2003**, *150*, A1457.
(3) For a review, see Kasavajjula, U.; Wang, C.; Appleby, A. J. *J. Power Sources* **2007**, *163*, 1003.
(4) Li, H.; Huang, X.; Chen, L.; Zhou, G.; Zhang, Ze; Yu, D.; Mo, Y. J.; Pei, N. *Solid State Ionics* **2000**, *135*, 181.
(5) Limthongkul, P.; Jang, Y. I.; Dudney, N. J.; Chiang, Y. M. *Acta Mater.* **2003**, *51*, 1103.
(6) Li, J.; Dahn, J. R. *J. Electrochem. Soc.* **2007**, *154*, A156.
(7) Key, B.; Bhattacharyya, R.; Morcrette, M.; Seznéc, V.; Tarascon, J.-M.; Grey, C. P. *J. Am. Chem. Soc.* **2009**, *131*, 9239.
(8) Key, B.; Morcrette, M.; Tarascon, J.-M.; Grey, C. P. *J. Am. Chem. Soc.* **2011**, *133*, 503.
(9) Kang, Y.-M.; Suh, S.-B.; Kim, Y.-S. *Inorg. Chem.* **2009**, *48*, 11631.
(10) Wan, W.; Zhang, Q.; Cui, Y.; Wang, E. *J. Phys.: Condens. Matter* **2010**, *22*, 415501.
(11) Peng, B.; Cheng, F.; Tao, Z.; Chen, J. *J. Chem. Phys.* **2010**, *133*, 034701.
(12) Zhang, Q.; Zhang, W.; Wan, W.; Cui, Y.; Wang, E. *Nano Lett.* **2010**, *10*, 3243.
(13) Zhang, Q.; Cui, Y.; Wang, E. *J. Phys. Chem. C.* **2011**, *115*, 9376.
(14) Chevrier, V. L.; Zwanziger, J. W.; Dahn, J. R. *Can. J. Phys.* **2009**, *87*, 625.
(15) Chevrier, V. L.; Zwanziger, J. W.; Dahn, J. R. *J. Alloys Compd.* **2010**, *496*, 25.
(16) Chevrier, V. L.; Dahn, J. R. *J. Electrochem. Soc.* **2009**, *156*, A454.
(17) Chevrier, V. L.; Dahn, J. R. *J. Electrochem. Soc.* **2010**, *157*, A392.
(18) Huang, S.; Zhu, T. *J. Power Sources* **2011**, *196*, 3664.
(19) Kim, H.; Chou, C. Y.; Ekerdt, J. G.; Hwang, G. S. *J. Phys. Chem. C* **2011**, *115*, 2514.
(20) Johari, P.; Qi, Y.; Shenoy, V. B. *Nano Lett.* **2011**, *11*, 5494.
(21) Obrovac, M. N.; Christensen, L. *Electrochem. Solid-State Lett.* **2004**, *7*, A93.
(22) Obrovac, M. N.; Krause, L. J. *J. Electrochem. Soc.* **2007**, *154*, A103.
(23) Kubota, Y.; Escaão, M. C. S.; Nakanishi, H.; Kasai, H. *J. Appl. Phys.* **2007**, *102*, 053704.
(24) Xu, Y. H.; Yin, G. P.; Zuo, P. *J. Electrochim. Acta* **2008**, *54*, 341.
(25) Beaulieu, L. Y.; Eberman, K. W.; Turner, R. L.; Krause, L. J.; Dahn, J. R. *Electrochem. Solid-State Lett.* **2001**, *4*, A137.
(26) Obrovac, M. N.; Christensen, L.; Le, D. B.; Dahn, J. R. *J. Electrochem. Soc.* **2007**, *154*, A849.
(27) Lestriez, B.; Bahri, S.; Sandu, I.; Roué, L.; Guyomard, D. *Electrochem. Commun.* **2007**, *9*, 2801.
(28) Magasinki, A.; Dixon, P.; Hertzberg, B.; Kvit, A; Ayala, J.; Yushin, G. *Nat. Mater.* **2010**, *9*, 353.
(29) Lee, J. K.; Smith, K. B.; Hayner, C. M.; Kung, H. H. *Chem. Commun.* **2010**, *46*, 2025.
(30) Chan, C. K.; Peng, H.; Liu, G.; McIlwrath, K.; Zhang, X. F.; Huggins, R. A.; Cui, Y. *Nat. Nanotechnol.* **2008**, *3*, 31.
(31) Goldman, J. L.; Long, B. R.; Gewirth, A. A.; Nuzzo, R. G. *Adv. Funct. Mater.* **2011**, *21*, 2412.
(32) Lee, S. W.; McDowell, M. T.; Choi, J. W; Cui, Y. *Nano Lett.* **2011**, *11*, 3034.
(33) Liu, X. H.; et al. *Nano Lett.* **2011**, *11*, 3312.
(34) Kresse, G.; Furthmüller, J. *Phys. Rev. B* **1999**, *54*, 11169.
(35) Kresse, G.; Joubert, D. *Phys. Rev. B* **1999**, *59*, 1758.
(36) Perdew, J. P.; Ernzerhof, M.; Burke, K. *J. Chem. Phys.* **1996**, *105*, 9982.
(37) Schlier, R. E.; Farnsworth, H. E. *J. Chem. Phys.* **1959**, *30*, 917.
(38) Chadi, D. J. *Phys. Rev. Lett.* **1979**, *43*, 43.
(39) Xu, G.; Deng, B.; Yu, Z; Tong, S. Y.; Van Hove, M. A. LBNL Paper LBNL-54667; Lawrence Berkeley National Laboratory: Berkeley, CA, 2004. Retrieved from: http://www.escholarship.org/uc/item/9m313721.
(40) Chan, M. K. Y; Wolverton, C. M.; Greeley, J. P. In preparation.
(41) Momma, K.; Izumi, F. *J. Appl. Crystallogr.* **2008**, *41*, 653.
(42) Sanchez, J. M.; Ducastelle, F.; Gratias, D. *Physica A* **1984**, *128*, 334.
(43) Aydinol, M. K.; Kohan, A. F.; Ceder, G.; Cho, K.; Joannopoulos, J. *Phys. Rev. B* **1997**, *56*, 1354.
(44) Malik, R.; Zhou, F.; Ceder, G. *Nat. Mater.* **2011**, *10*, 587.
(45) Long, B.; Chan, M. K. Y.; Greeley, J. P.; Gewirth, A. A. *J. Phys. Chem. C* **2011**, *115*, 18916.
(46) Beaulieu, L. Y.; Hatchard, T. D.; Bonakdarpour, A.; Fleischauer, M. D.; Dahn, J. R. *J. Electrochem. Soc.* **2003**, *150*, A1457.
(47) Qiu, X.; Thompson, J. W.; Billinge, S. J. L. *J. Appl. Crystallogr.* **2004**, *37*, 678.
(48) Nesper, R.; von Schnering, H. G.; Curda, J. *Chem. Ber.* **1986**, *119*, 3576.
(49) Frank, U.; Mueller, W.; Schaefer, H. *Z. Naturforsch., B: Anorg. Chem., Org. Chem.* **1975**, *30*, 10.
(50) Nesper, R.; von Schnering, H. G. *J. Solid State Chem.* **1987**, *70*, 48.
(51) Gladyshevskii, E. I.; Oleksiv, G. I.; Kripyakevich, P. I. *Kristallografiya* **1964**, *9*, 338.
(52) Nosé, S. *J. Chem. Phys.* **1984**, *81*, 511.
(53) Eaglesham, D. J.; et al. *Phys. Rev. Lett.* **1993**, *70*, 1643.
(54) Fister, T.; Schmidt, M.; Johnson, C. S.; Slater, M.; Shirley, E.; Chan, M. K. Y.; Fenter, P. *J. Chem. Phys.* **2011**, *135*, 224513.
(55) Sangster, J.; Pelton, A. D. *J. Phase Equilib.* **1997**, *18*, 289.
(56) Henkelman, G.; Uberuaga, B. P.; Jonsson, H. *J. Chem. Phys.* **2000**, *113*, 9901.
(57) Vasp TST Tools Home Page. http://theory.cm.utexas.edu/vtsttools/.
(58) Lide, D. R., Ed. *CRC Handbook of Chemistry and Physics*; CRC Press: Boca Raton, FL, 2004, pp 12−108.
(59) Donovan, E. P.; Spaepen, F.; Turnbull, D.; Poate, J. M.; Jacobson, D. C. *J. Appl. Phys.* **1985**, *57*, 1795.
(60) Bernstein, N.; Aziz, M. J.; Kaxiras, E. *Phys. Rev. B.* **1998**, *58*, 4579.
(61) Durandurdu, M; Drabold, M. D. *Phys. Rev. B.* **2003**, *67*, 212101.
(62) We produce amorphous Si by heating crystalline Si with Tersoff potential to 3000 K, and then quenching with ab initio molecular dynamics (DFT-PBE) at 1000 K. The amorphous Si sample is then relaxed with DFT-PBE, and we find its energy to be 0.27 eV/atom higher than crystalline Si.
(63) Gao, B.; Sinha, S.; Fleming, L.; Zhou, O. *Adv. Mater.* **2001**, *13*, 816.